Sādhanā (2020)45:217
https://doi.org/10.1007/s12046-020-01456-5

Modeling serrated flow of SS 316L under dynamic strain aging effect

SIDDHARTHA PATRA*, SANKAR DHAR and SANJIB KUMAR ACHARYYA

Department of Mechanical Engineering, Jadavpur University, Kolkata 700032, India
e-mail: siddharthapatra16@gmail.com

MS received 13 April 2018; revised 21 April 2019; accepted 10 January 2020

Abstract. The serrated behavior of the stress-strain curves also known as PLC effect due to dynamic strain aging of SS 316L is investigated here from room temperature to 550°C. Tensile tests were conducted for strain rates $10^{-5}-10^{-2}$/s. Serrations of type D, type A and type A+B were observed at different loading conditions. A material model was fitted to the experimental data to simulate the serrated flow in the stress strain diagrams. For this an approach similar to a previous study done with an Al-Mg alloy was followed. However, few changes in the analysis steps were performed to accommodate temperature dependency, a feature not addressed in the earlier work. In addition, the fitment technique was improvised so that the material model could be fit through a substantially smaller set of experimental data, thus improving the speed of the fitting process. Finally, comparisons were done between the experimental data and the results from the simulations. Critical strains from the simulations were found to be of the same order of magnitude of the experimental critical strains and the serrations could also be found in the simulated stress-strain diagrams similar in some aspects to the experimental serrations.

Keywords. Dynamic strain aging; critical strain; DSA band; PLC effect.

1. Introduction

Dynamic strain aging or DSA effect in metallic materials such as ferrous and aluminum alloys results from the interaction of the mobile dislocations with the surrounding solute atoms (Beukel [1]). This results into certain average waiting time t_w for the mobile dislocation before it moves to the next pinning location. As a result, serrations are observed in the stress-strain curve. This is commonly known as Portevin-Le Chatelier (PLC) effect. DSA is characterized by a negative strain rate sensitivity, strain rate sensitivity (SRS) being measured at a given temperature and strain as-

$$S := \left.\frac{\partial \sigma}{\partial \ln \dot{\varepsilon}}\right|_{T,\varepsilon} \tag{1}$$

In combination with viscoplasticity, this causes strain rate instability [2] as opposed to plastic strain instability which is observed at the ultimate stress value in a tensile test. The plastic strain instability condition is given by the following criterion.

$$\Theta - \sigma \leq 0 \tag{2}$$

where, $\Theta := \left.\frac{\partial \sigma}{\partial \varepsilon}\right|_{\dot{\varepsilon}}$.

The strain rate instability is manifested as the serrations in the stress-strain diagram. However, such serrated behavior of the stress-strain plot is only observed after attainment of a given amount true plastic strain namely critical strain or ε_{cr} [3].

1.1 *Constitutive models for DSA*

Over the years a number of attempts have been made by authors to present constitutive models for DSA behavior. Bodner and Rosen [4] used a dry friction model to explain the stepped stress-strain behavior of annealed and commercially pure aluminum. They argued that in dry friction the coefficient of kinetic friction μ_k is dependent on the relative velocity v_r. At higher range of velocities μ_k increases with v_r and at the lower range the reverse happens. This reverse behavior is characteristic to DSA. Penning [5] suggested a phenomenological model thus by assuming a negative "strain rate hardening" in the DSA strain rate range. Kubin *et al* [6] uses the concept of negative strain rate sensitivity to give a closed-form solution that predicts discontinuous deformation.

Typically the DSA stress is modeled as a nonlinear isotropic hardening stress such as the simple model presented

This paper is a revised and expanded version of an article presented in "First International Conference on Mechanical Engineering" held at 'Jadavpur University', Kolkata, India during January 4–6, 2018 (INCOM-2018).

*For correspondence

Published online: 31 August 2020

by Yaguchi and Takahashi [7] given by the following equation.

$$\dot{R}_a = b(Q_a - R_a)\dot{\varepsilon}_p, \tag{3}$$

where, the asymptotic value of the DSA stress is $Q_a = A + B\ln\dot{\varepsilon}_p$ and $b = b_1$ if $R_a < Q_a$ and $b = b_2$ if $R_a > Q_a$. A model like this one would predict the occurrence of critical strain where the strain rate sensitivity vanishes, i.e., $S = 0$ while $\Theta - \sigma > 0$.

A phenomenological model based on dislocation dynamics is popular with many authors such as McCormick [8], Zhang *et al* [9], Maziere and Diereke [10] and Chaboche *et al* [11] with minor variations. This model uses the concept of an internal variable called the aging time, t_a whose rate of change has the following expression.

$$\dot{t_a} = 1 - \frac{t_a}{t_w} \tag{4}$$

where, t_w is the average waiting time of the dislocations in a locked position. The asymptotic value of aging time t_w is a function of strain rate and strain and has the following expression.

$$t_w = \frac{\Omega(\varepsilon_p)}{\dot{\varepsilon}_p} \tag{5}$$

Finally the aging stress, R_a is a function of the aging time, t_a and the accumulated plastic strain, ε_p. Zhang *et al* [9] used the following functional forms for $\Omega(\varepsilon_p)$.

$$\Omega = \omega_1 + \omega_2\varepsilon_p^{\beta} \tag{6}$$

where, $\omega_1, \omega_2, \beta$ are material parameters. The aging stress, R_a was represented as following.

$$R_a = C_m\left[1 - \exp\left(-P_2\varepsilon_p^{\alpha}t_a^{n}\right)\right] \tag{7}$$

where, C_m is the saturation value and P_2, α, n are material parameters.

The total uniaxial stress can be divided into following parts.

$$\sigma = \sigma_y + R + R_a + \sigma_v \tag{8}$$

Here, σ_y is the yield stress. R is the rate independent strain hardening stress. R_a is the DSA stress and σ_v is the rate dependent viscoplastic stress.

Maziere and Diereke [10] in their work with an Al-Mg alloy AA5754, presented different criteria for the prediction of critical strain. In order to discuss them, we need to define the following quantities. The instantaneous SRS, S_i is defined by Eq. (9) and represents strain rate sensitivity of the viscoplastic part of the stress.

$$S_i = \left.\frac{\partial\sigma_v}{\partial\ln\dot{\varepsilon}_p}\right|_{T,\varepsilon_p} \tag{9}$$

The aging SRS, S_a is defined by Eq. (10) and represents the strain rate sensitivity of the aging stress.

$$S_a = -\left.\frac{\partial R_a}{\partial\ln t_a}\right|_{\varepsilon_p,T} = \left.\frac{\partial R_a}{\partial\ln\dot{\varepsilon}_p}\right|_{\varepsilon_p,T} \tag{10}$$

Thus,

$$S = S_i + S_a. \tag{11}$$

S is regarded as the steady state SRS. The simplest criterion for detecting the critical strain is $S \le 0$. This criterion however under predicts critical strain. On linearization the system equation is obtained in the form of Eq. (12).

$$\begin{bmatrix}\delta\dot{\varepsilon}_p\\ \delta\dot{t_a}\end{bmatrix} = [\boldsymbol{M}]\begin{bmatrix}\delta\varepsilon_p\\ \delta t_a\end{bmatrix} \tag{12}$$

where,

$$\boldsymbol{M} = \frac{\dot{\varepsilon}}{S_i}\begin{bmatrix}\sigma - \Theta & \frac{S_a}{t_a}\\ \frac{t_a}{\Omega}(\Theta - \sigma) & -\frac{1}{\Omega}(S_i + S_a)\end{bmatrix} \tag{13}$$

By doing perturbation analysis (Eq. (12)) the authors predicted two more instability criteria given by Eqs. (14)-(15).

$$S_{OGC} = tr(\boldsymbol{M}) \le 0 \tag{14}$$

$$S_{EGC} = tr(\boldsymbol{M}) + 2\sqrt{\det(\boldsymbol{M})} \le 0 \tag{15}$$

The above criteria are based on the eigenvalues of the system matrix $\boldsymbol{M}$. S_{OGC} or oscillating growth criterion is the criterion based on the eigenvalues being complex with positive real part so that the perturbations have growing oscillating evolution and S_{EGC} or exponential growth criterion is the criterion based on the eigenvalues being real and positive so that the perturbations have growing exponential evolution. S_{EGC} was found out to be the most accurate criterion for the prediction of critical strains. Based on the strains corresponding to equality of a given criterion the different criteria can be listed as follows.

$$\Theta - \sigma > S_{EGC} > S_{OGC} > S \tag{16}$$

In order to fit the material parameters they conducted several FE simulations on a single Gauss point and checked for the minimization of the following function.

$$\Pi^* = \sum_{i=1}^{n_{SR}}\left(w_c\left(\varepsilon_{cr}^{FE} - \varepsilon_{cr}^{Expt}\right)^2 + w_\sigma\sum_{j=1}^{1000}\left(\sigma_j^{FE} - \sigma_j^{Expt}\right)^2\right) \tag{17}$$

where, w_c, w_σ were the weights assigned to critical strain and stress values. n_{SR} in Eq. (17) represents number of different strain rates. For the fitting operation, 1000 data

points were extracted from stress-strain curve at each strain rate.

The diffusion of solute atoms causing the DSA behavior in metallic alloys are associated with activation energies which are characteristic to the material of the solute atoms and also the type of the solute atom, i.e., interstitial or substitutional. Thus, by determining the activation energy, one can also get an idea of the solute element diffusion of which is causing the DSA. Gopinath *et al* [12] presented a detailed study on determining the activation energy associated with such diffusion and their correlation with the critical strain. Material undergoing DSA may exhibit negative strain rate sensitivity or direct PLC effect or a reverse PLC effect. Under direct PLC effect the critical strain has the following relationship with the temperature and strain rate involving the activation energy.

$$\dot{\varepsilon}_p = A\varepsilon_{cr}^{m+\beta} \exp\left(-\frac{Q_{act}}{R_g T}\right) \tag{18}$$

Thus under direct PLC effect the critical strain decreases with decrease in strain rate and increases with decrease of temperature, i.e., critical strain is smaller if the DSA effect is more severe. However, Eq. (18) can only be applied for direct PLC effect and for reverse PLC effect the authors presented the following expression.

$$Q_{act} = -R_g \left[\frac{\partial \ln \dot{\varepsilon}}{\partial\left(\frac{1}{T}\right)}\right]_{\Delta\sigma,\varepsilon}, \tag{19}$$

where, $\Delta\sigma$ is the increment of stress based on the stress vs. strain rate plots at constant temperature and strain.

1.2 *Application and DSA behavior of 316L in literature*

Austenitic stainless steel variant 316L is used in nuclear power plants for piping networks [13, 14]. Typical service temperature for 316L is between 450-600°C. The material is subjected to thermo-mechanical loading due to thermal transient and stratification. Experimental studies revealed that the material experiences (DSA) in the said temperature range [15–23]. Muhamed *et al* [15] conducted tensile tests on SS 316L on as-received and as-welded conditions between 25-800°C and reported 500°C to be the peak aging temperature. Hong and Lee [16] conducted tensile and LCF tests on cold worked 316L between 20 and 750°C and strain rates $10^{-4}-10^{-2}$/s. DSA was observed between temperatures 250 and 600°C through negative strain rate sensitivity. There was change in the strength and ductility of the material within the DSA regime. Shastry *et al* [17] conducted tensile tests on 316L(N) between 25-750°C and strain rates $3 \times 10^{-5}-1.2 \times 10^{-3}$/s. Serrations were observed between 250 and 650°C. Gupta *et al* [18] conducted tensile tests on 316 stainless steel from room temperature to 650°C for strain rates $10^{-4}-10^{-3}$/s. DSA was observed above 350°C at 10^{-4}/s and all strain rates above 400°C. Artificial neural network method was used to model the DSA behavior. Jiang *et al* [19] conducted stress controlled fatigue-creep test on hot rolled and DSA pre-treated 316L at 550°C. DSA was manifested as mean stress abrupt jump for both the type of materials. Karlsen *et al* [20] conducted tensile tests on 316L at 200°C, 288°C, 400°C at strain rate 10^{-5}/s. Serrated behavior was observed at 288°C and 400°C. Pham *et al* [21] reported DSA of 316L at 300°C. Hong and Lee [22] reported the DSA behavior 316L at 250-550°C and strain rates $10^{-4}-10^{-2}$/s. Three different activation energies were observed to be associated with serrated flow of 316L. This indicates that the DSA of 316L is caused by diffusion of more than one type of solute and substitutional atoms. Puchi-Cabera [23] studied the mechanical behaviors of 316L between temperatures 600°C and 850°C between strain rates 10^{-3}/s to 10^{2}/s. They reported that the DSA behavior with negative strain rate sensitivity was observed between temperatures 600°C and 800°C and strain rates 0.1−10/s.

Although so much studies have been conducted on 316L, not many of them have attempted to identify a constitutive model which can represent the DSA behavior of the material over a wide range of temperature and strain rate. In the present study we would like to address this problem.

2. Experimental observations

Tensile tests were conducted on the ASTM E8/E8M specimen in Instron 5582 UTM (Max. load = 100 kN) from room temperature to 550°C for strain rates 0.01/s, 0.001/s, 0.0001/s and 1E−5/s. The composition of the material is given in table 1.

Dimensions of the specimen are given in figure 1. The gauge length of the extensometer was 25 mm. The accurate measurements of strain were done using the extensometer up to a total engineering strain of 10%. The extensometer was removed thereafter to avoid damage of the instrument due to possible breaking of the test specimen. The strain beyond this value is calculated approximately from the relative displacement of the grips. Therefore in this analysis maximum displacement amounting to 10% of total engineering strain is considered.

Table 1. Composition of SS 316L.

C	Si	Mn	P	S	Cr	Mo	Ni	Fe
0.018	0.55	1.4	0.032	0.008	16.05	2.05	10.11	Rest

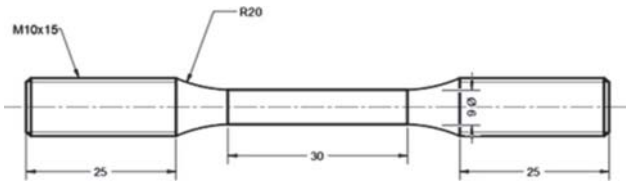

Figure 1. Tensile specimen.

2.1 *Identification of DSA strain rates and temperatures and critical strains*

Figure 2(a) shows the stress-strain diagrams for the loading conditions showing DSA behavior. At strains below 10%, serrations were observed only at temperatures 550°C, 500°C and 450°C. At 550°C serrations were observed at three strain rates, 0.001/s, 0.0001/s, 1E−5/s. At 500°C serrations were observed at strain rates 0.0001/s and 1E−5/s. At 450°C serrations were observed at only one strain rate, 1E−5/s.

The stress-strain diagrams for all such loading conditions are shown in the following figure with each curve with an offset of 50 MPa from the previous one for better visualization. The thick line marks the critical strain for each loading condition. The critical strains are determined by a Matlab code that detects the critical strain as the strain at which a stress depression of minimum 0.2 MPa occurs for the first time. The choice of the threshold value of the stress is obtained through trial and error and optimized to be small enough to determine critical strain accurately yet big enough to ignore the noise from the UTM. Venkadesan *et al* [24] used a closely similar approach for the detection of critical strains for different strain rates and temperatures.

2.2 *Identification of types of serrations*

The types of serrations [25, 26] observed for the above loading conditions are identified in figure 2(b).

Types of serrations depend on the temperature and the strain rate [27, 28]. The diffusion rate of solute atoms is dependent upon the temperature whereas the dislocation velocity is dependent upon the applied strain rate. For instance, at a given temperature, say 550°C, the mobility of the solute atoms is same at the different strain rates, say 10^{-4}/s and 10^{-5}/s, but the dislocation velocities are different. At 10^{-4}/s the mobility of the dislocations is higher compared mobility of the solute atoms. Thus, the pinning mechanism is partial. This slows down the dislocations at the obstacles and more solute atoms entre into the dislocation cloud to make the pinning process complete. This process is followed by the unpinning of the dislocations. Thus PLC process has three mechanisms, namely partial pinning, pinning and unpinning. This results in the serrations of type A. At 10^{-5}/s the dislocations move slowly. Hence partial pinning mechanism is less observable. This results into a transition from serrations of type A to type B, namely type A+B.

Keeping the strain rate constant at 10^{-5}/s, if the temperature is reduced to 500°C from 550°C, the same observation is repeated. At a lower temperature, the mobility of the solute atoms is reduced and once again the dislocation mobility is higher than the solute atoms thereby producing serrations of type A.

Type D serrations were observed at 550°C at strain rate 10^{-3}/s, at 500°C at strain rate 10^{-4}/s and 450°C at strain rate 10^{-5}/s. At these loading conditions the dislocation mobility is much higher compared to the mobility of the solute atoms. Thus producing plateaus in the stress-strain diagram with no significant work hardening or strain gradient [25].

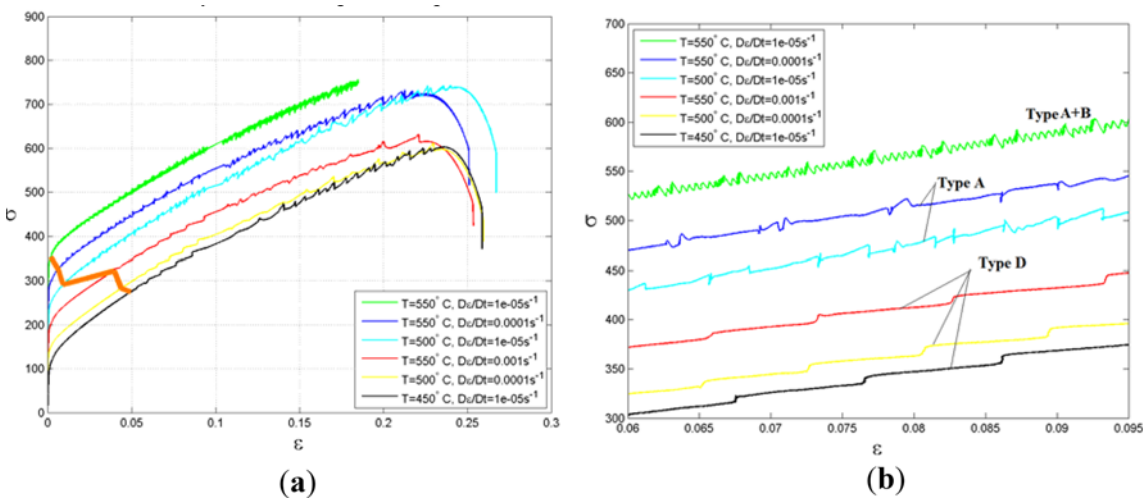

Figure 2. Stress-Strain diagrams for different loading cond (Stresses in MPa). (**a**) Stress strain diagrams superimposed with critical strains. (**b**) Types of serrations for different loading conditions.

2.3 *Calculation of activation energy*

In our case direct PLC effect was observed which can be confirmed from figures 3-4. Figure 3 shows the variation of critical strain with strain rate at constant temperatures. From Eq. (18) we have-

$$\ln \dot{\varepsilon}_p = \ln A + (m+\beta)\ln \varepsilon_{cr} - \frac{Q_{act}}{R_g T} \tag{20}$$

$$\Rightarrow \ln \dot{\varepsilon}_p = (m+\beta)\ln \varepsilon_{cr} + A'(T) \tag{21}$$

Thus if temperature remains constant, plots of logarithm of strain rate vs. logarithm of critical strain according to the above relation should be straight lines with slopes equal to $m+\beta$. Here we got an average value of the parameter $m+\beta = 1.33$. This value being higher than unity, is an indication of the diffusion of substitutional solute atoms.

Figure 4 shows the variation of critical strain at constant strain rates with the temperature. If the strain rate is kept constant we have the following linear relationship between the logarithm of critical strain and the inverse of temperature.

$$\ln \varepsilon_{cr} = \frac{Q_{act}}{R_g T(m+\beta)} + A''(\dot{\varepsilon}_p) \tag{22}$$

Thus, the slopes of the plots would yield the $\frac{Q_{act}}{R_g(m+\beta)}$ values. Thus, the activation energy can be evaluated using the following relation.

$$Q_{act} = R_g(m+\beta)\frac{\partial \ln \varepsilon_{cr}}{\partial\left(\frac{1}{T}\right)}\bigg|_{\dot{\varepsilon}_p} \tag{23}$$

From the plots we got an average value $\frac{\partial \ln \varepsilon_{cr}}{\partial\left(\frac{1}{T}\right)}\Big|_{\dot{\varepsilon}_p} = 24080$. Using the above relations we can approximately determine the activation energy associated with the DSA effect to be 266 kJ/mol. This is close to the activation energy of chromium for lattice diffusion in γ-iron (FCC) as reported by Bowen and Leak [29] and chromium is also the major alloying component. Thus, we ascertain that the diffusing element is chromium which is causing the DSA phenomenon.

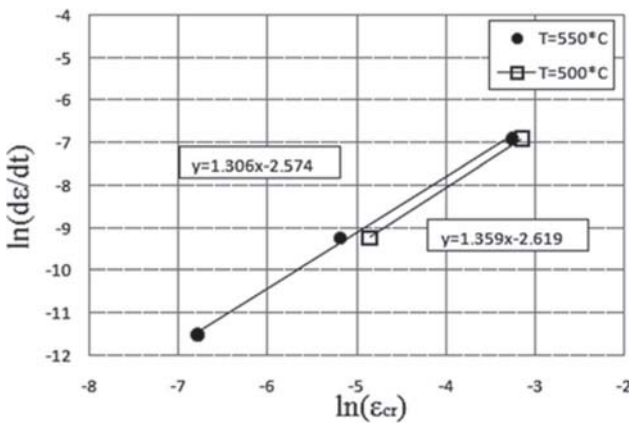

Figure 3. Critical strain vs. strain rate.

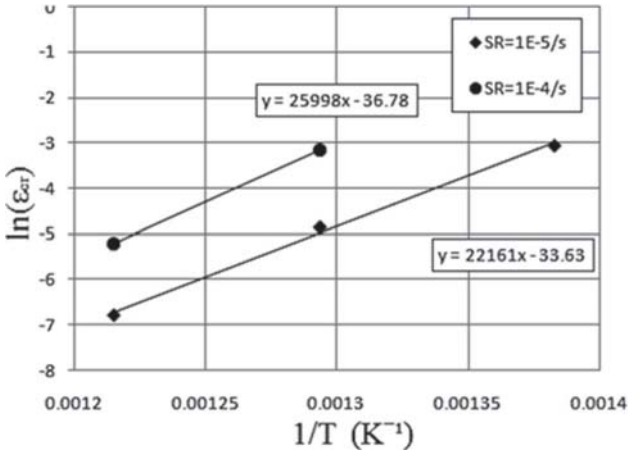

Figure 4. Critical strain vs. temperature.

3. Details of the material model

Following the approach of Maziere *et al* [10] a material model was fit to the experimental data. The expression for t_w is simplified into a linear form given by Eq. (24).

$$t_w = \frac{c_0 + c_1 \varepsilon_p}{\dot{\varepsilon}_p} \tag{24}$$

The above expression was further simplified by taking $c_1 = 0$ for the ease of fitment to the experimental data. The evolution of the aging time t_a is guided by Eq. (4). In the end the expression for the aging stress is given by Eq. (25).

$$R_a = c_5\left(1 - \exp\left(-c_2 \varepsilon_p^{c_3} t_a^{c_4}\right)\right) \tag{25}$$

The c_5 parameter is considered to be temperature dependent.

3.1 *Fitting of material parameters*

Genetic Algorithm routine from the optimization toolbox of MATLAB was used to fit the material parameters. The criterion used to fit the material model to the experimental data is represented through Eq. (26).

$$\underset{c_j}{minimize}\ \Pi := \sum_{i=1}^{n}\left(\sigma_i^{expt} - \sigma_i^{fit}(c_j)\right)^2 \tag{26}$$

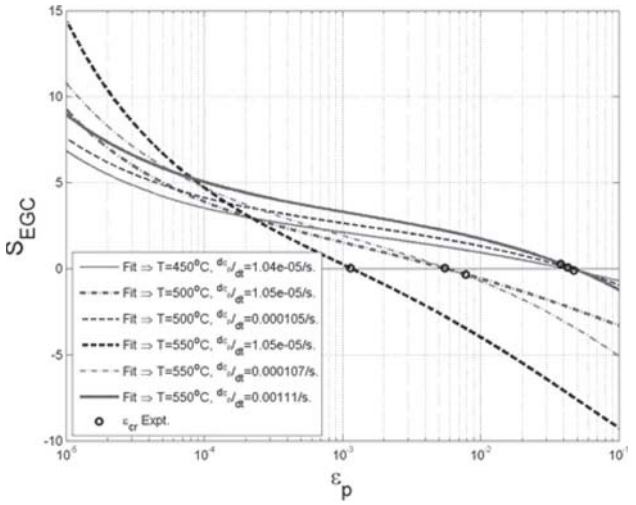

Figure 5. Approximate S_{EGC} vs. plastic strain plot from Matlab fit by taking $t_a \approx t_w$, superimposed with experimental critical strains used to get an estimation of goodness of fit. The plot distinguishes loading conditions into first, second and third tiers.

Significance of the criterion is to minimize the squared difference of the experimental stress values to the stress values corresponding to fitted material model. Here c_j represents the set of DSA parameters and i represents individual stress-strain data points where n is the total number of data points. Maziere *et al* [10] considered 1000 points for each stress-strain plot in order to fit DSA model. Here only four data points corresponding to 3%, 5%, 7% and 9% true plastic strain were used for each stress-strain diagram within the DSA affected temperature strain rate range. This approach was used to reduce the time required for fitting material parameter to the experimental data from a wide range of temperature and strain rate.

The above objective function was subjected to the non-linear constraint given by Eq. (27).

$$\left|\overline{S_{EGC}\left(c_j, \varepsilon_{cr}\right)}\right| - 0.1 < 0 \tag{27}$$

The significance of the above criterion was to restrict the average of the absolute values of the S_{EGC} for the different loading conditions at the respective critical strain within 0.1. Once the material parameters were obtained from the fit, as an intermediate checking of the goodness of the fit, a separate Matlab script was written to plot S_{EGC} values for different loading conditions over a strain range of $10^{-4}-0.1$, superimposed with respective experimentally obtained critical strains. The plots are shown in figure 5. From the plots it can be seen that S_{EGC} values for individual loading conditions are very close to zero at their respective critical strains. The aging time t_a was approximated to be t_w for the simplicity of the calculations.

From figures 3 and 5, the loading conditions can be classified into three categories based on the intensity of the serrated behavior observed in the stress-strain diagram. The categories are listed in table 2. The first tier loading conditions are associated with an early occurrence of the serrations, i.e., low critical strain (<1%) and a high frequency of (in terms of strain) serrations. The second tier loading conditions are associated with critical strain close to 1% and medium frequency of serrations. The third tier loading conditions are associated with critical strains above 4% and low frequency of serrations.

Table 2. Categorization of loading conditions on the basis of serrated flow.

	$T = 450°C$	$T = 500°C$	$T = 550°C$
First Tier	-	-	$\dot{\varepsilon} = 1.0E{-}5$/s
Second Tier	-	$\dot{\varepsilon} = 1.0E{-}5$/s	$\dot{\varepsilon} = 1.0E{-}4$/s
Third Tier	$\dot{\varepsilon} = 1.0E{-}5$/s	$\dot{\varepsilon} = 1.0E{-}4$/s	$\dot{\varepsilon} = 1.0E{-}3$/s

Table 3. Parameters for DSA model.

Parameter	Value
c_0	9.0E−5
c_1	0
c_2	0.565
c_3	0.274
c_4	0.370

3.2 *DSA parameters*

The material parameters are selected when satisfactory fit was observed. The DSA parameters are listed in table 3.

The temperature dependent c_5 parameter was determined for all temperatures and an approximate relation, given by

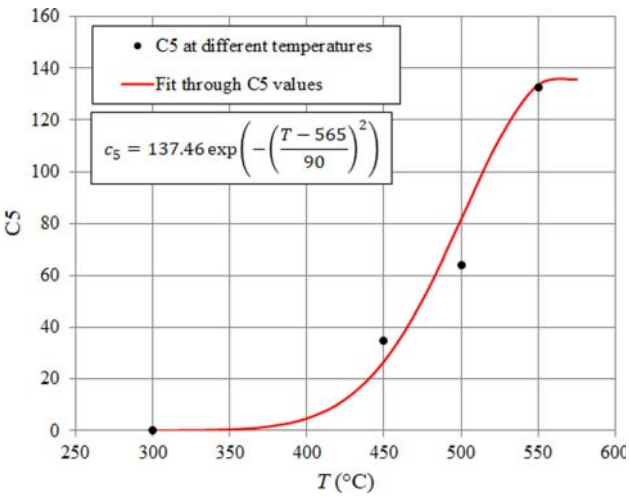

Figure 6. Variation of c_5 with temperature.

Eq. (28), was fit through those values as could be seen from figure 6.

$$c_5 = 137.46 \exp\left(-\left(\frac{T-565}{90}\right)^2\right) \tag{28}$$

4. Numerical analysis

The material model was implemented through a standard package (ABAQUS UMAT) and simulations were conducted on a cylindrical geometry. The length of the cylindrical geometry was taken to be 25 mm and the diameter was taken 6.0 mm. These dimensions were used to represent the test region in the tensile specimen, i.e., the segment of the tensile specimen between the two arms of the extensometer. The back end of the cylindrical geometry was provided with the rigid body constraint and the tensile load was applied at the front as could be seen from figure 7(a). In addition an initial stress perturbation was provided to one of the elements to cause an initial imperfection, thus facilitating strain localization. The value of the stress perturbation used was 10 MPa similar to Zhang *et al* [9]. The sensitivity of the results on the initial stress perturbation has not been considered for the current study and may be addressed in a future communication. The initial stress distribution with only one element with a stress perturbation is shown in figure 7(b). Simulations were run by taking 0.1% of strain increment per step, in order to capture the nature of the stress-strain curve.

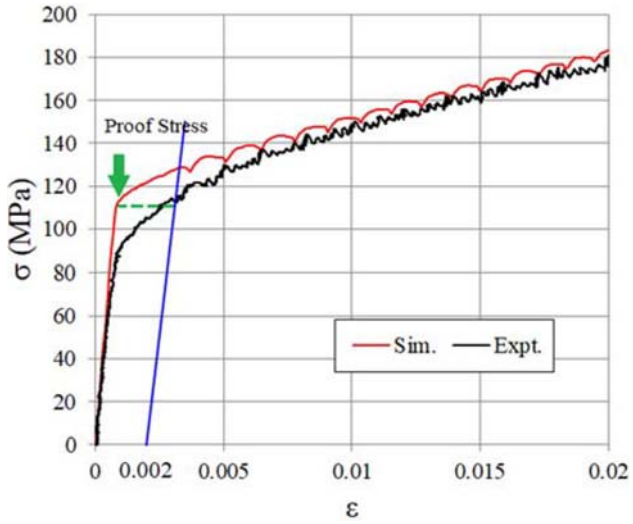

Figure 8. Horizontal gap between stress strain plots of experimental vs. simulation resulting from the use of proof stress as the yield stress.

5. Results and discussion

For each temperature, the lowest proof stress for different strain rates was used as the yield stress. This resulted in an initial offset from the experimental stress-strain diagrams and the same from the simulations as could be seen from figure 8.

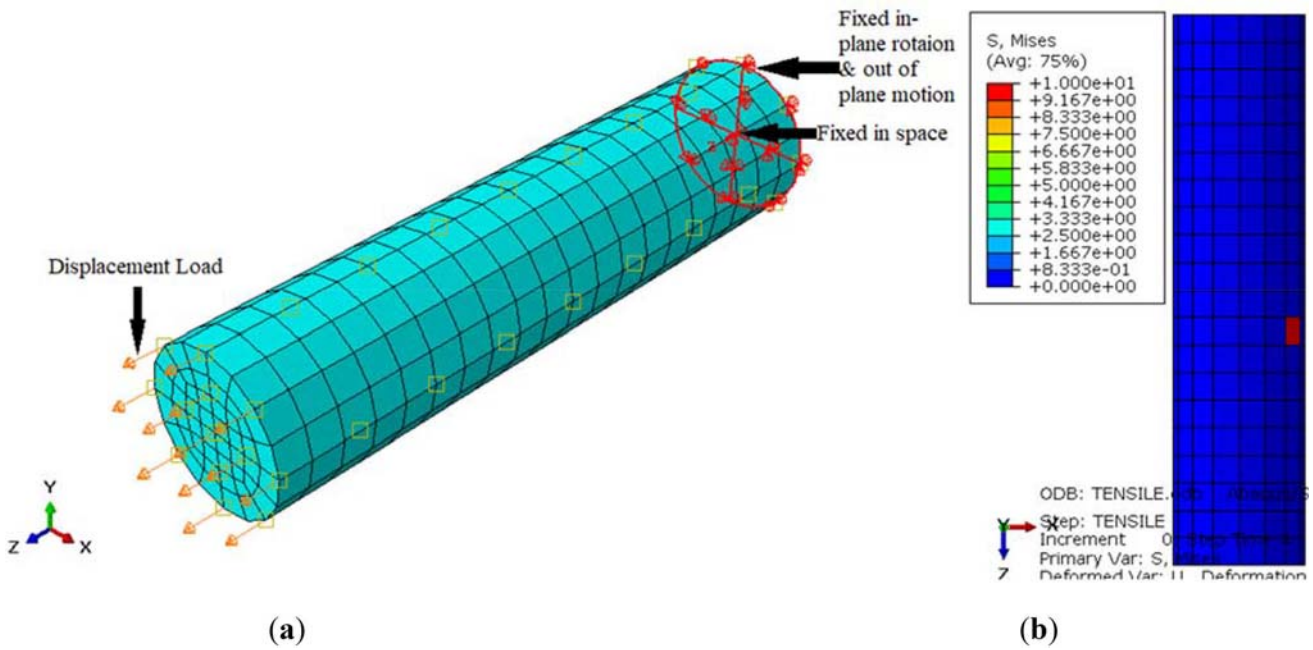

Figure 7. Boundary Conditions and Loads. (**a**) Mesh and BCs showing rigid body constraint at the back end and nonzero displacement load at the front. (**b**) Initial stress perturbation of 10 MPa at a single element.

5.1 *Comparison of the stress-strain diagrams*

Figure 9 shows both experimental and simulated stress strain diagrams for different strain rates at 550°C. At 550°C, different types of DSA behaviors are observed at different strain rates. For the strain rate of 10^{-2}/s, stress-strain diagram shows no serration. For $\dot{\varepsilon} = 10^{-3}$/s, low frequency (with respect to strain) serrations are observed after a strain of 4%. For $\dot{\varepsilon} = 10^{-4}$/s, medium frequency of serrations are observed from approximately 1% of strain. For $\dot{\varepsilon} = 10^{-5}$/s, high frequency of serrations is observed from a very small strain (<1%). The stress-strain curves for different loading conditions reveal that although the exact features of the serrations do not closely match, the serration from experimental results and simulations show similarity in terms of the frequency, amplitude and first occurrence of the serrations. This shows that although the material

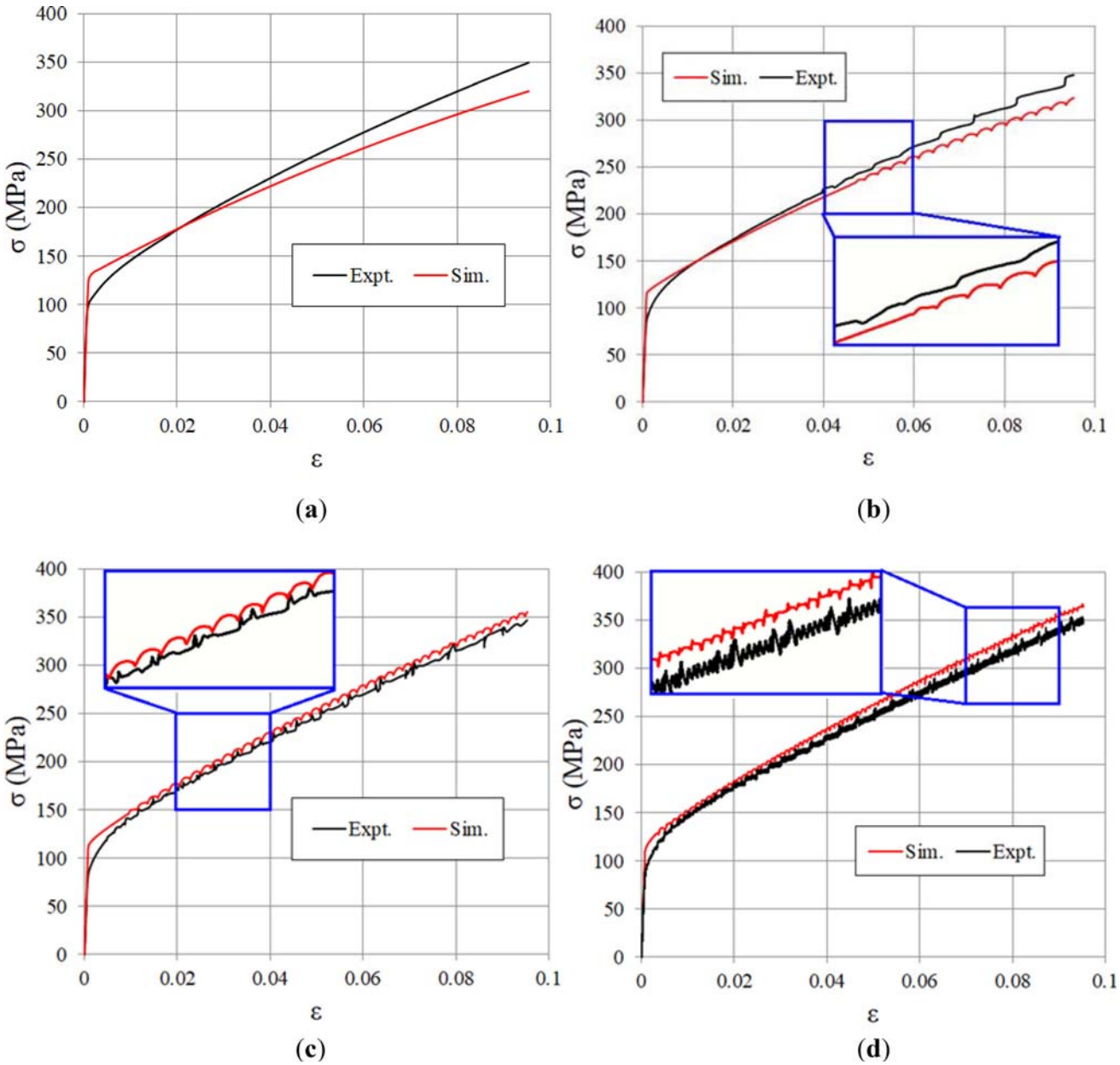

Figure 9. Experimental vs. Simulation true stress-strain plots at 550°C, showing different levels of serrated behavior at different strain rates. (**a**) No serrations at $\dot{\varepsilon} = 0.01$/s. (**b**) Low frequency serrations observed above 4% strain at $\dot{\varepsilon} = 0.001$/s. (**c**) Medium frequency serrations are observed above 1% strain at $\dot{\varepsilon} = 0.0001$/s. (**d**) High frequency serrations are observed to start below 1% strain at $\dot{\varepsilon} = 1.0E{-}5$/s.

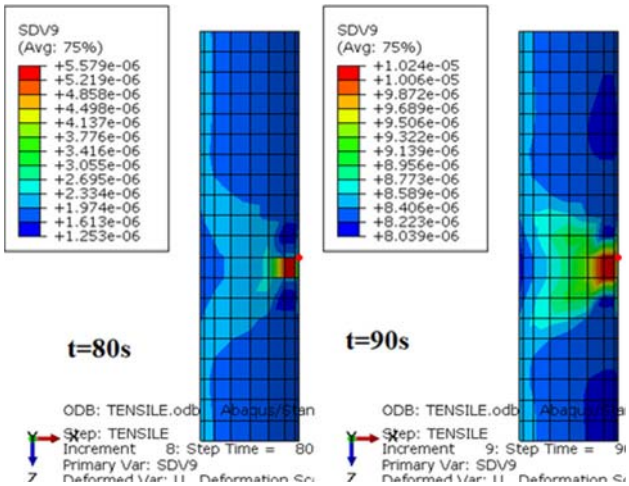

Figure 10. Evolution of strain rate distribution for the loading condition $T = 450°C$ and $\dot{\varepsilon} = 1.0E-5/s$ showing initial variation in strain rate growing into uniform distribution.

parameters were fitted by taking only a small number of stress-strain points, the DSA behavior of the material could be captured.

This also shows that the proposed material model through the employed curve fitting can be effectively used to model the material behavior for both DSA and non-DSA ranges of loading conditions.

5.2 *Periodic strain-rate variation*

Figure 10 shows distribution of plastic strain rate over the geometry at the early stage of plastic deformation. The plots are shown for the loading condition, 450°C temperature and a strain rate of 10^{-5}/s. Since, one of the elements is provided with a stress perturbation, the strain rate is initially high in the neighborhood. With time this distribution becomes more uniform. Also, the uniform value

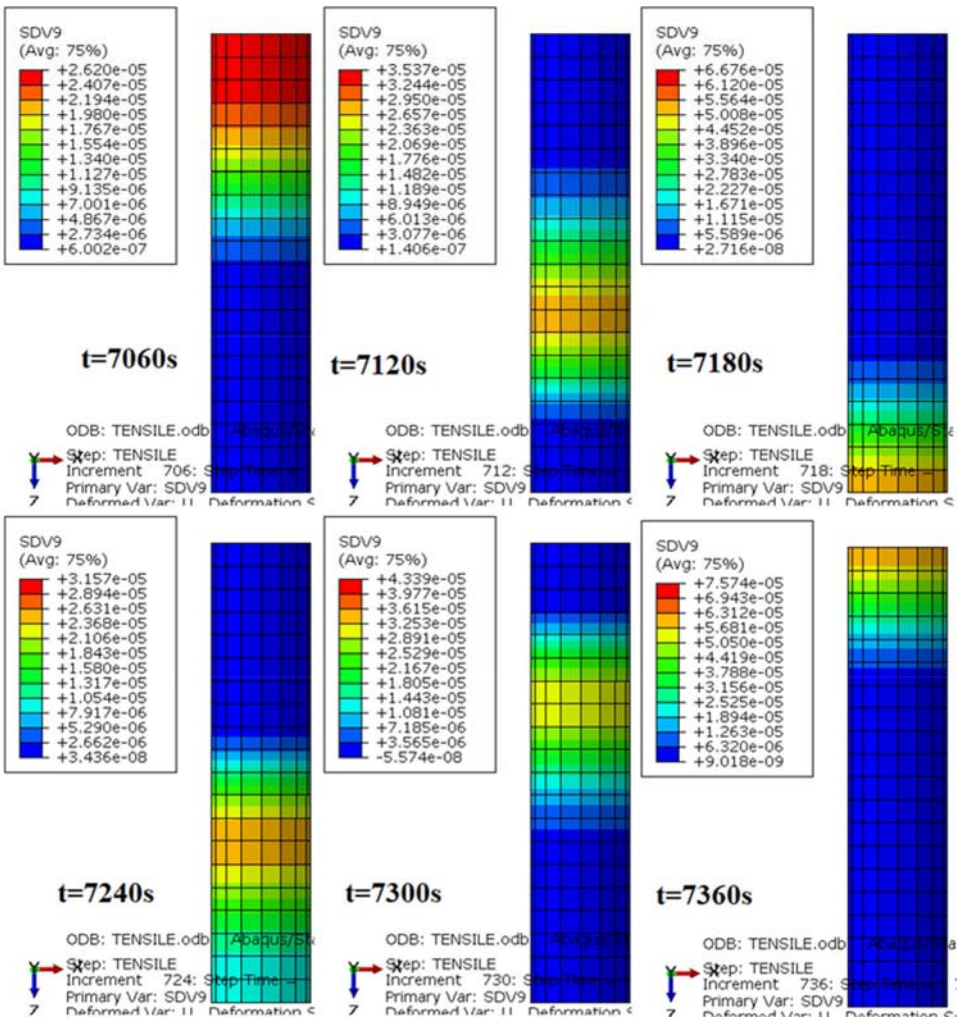

Figure 11. Periodic variation of strain rate over the geometry is associated with the serrations in the stress-strain diagram. Showing the first cycle.

Table 4. Critical strains experiment vs. simulation.

Temp. (T)	450°C	500°C		550°C		
Strain Rate ($\dot{\varepsilon}$)	1.0E−5/s	1.0E−4/s	1.0E−5/s	1.0E−3/s	1.0E−4/s	1.0E−5/s
Critical Strain (ε_{cr}) Expt.	0.0472	0.0427	0.00784	0.0382	0.00553	0.00114
Critical Strain (ε_{cr}) Sim.	0.07	0.029	0.005	0.047	0.0094	0.0035

approaches the applied strain rate (based on the length of the geometry) at the front face.

The uniformity of the distribution perturbed at a later stage and DSA bands were formed (figure 11). The DSA bands were found to be parallel to the circular faces. Zhang *et al* [9] and Bohlke *et al* [30] reported unidirectional flow of DSA bands. However, in the current study oscillatory flows were observed, i.e., the DSA bands would propagate from one face of the geometry to the other and return, as could be seen from figure 11. Apparently such oscillatory motion of the DSA bands are associated with the serrated nature of the stress-strain curves and the initiation of the oscillatory motion coincides with the critical strain obtained from the simulation as could be verified by comparing the time from figure 11 and the value of the critical strain from table 4.

5.3 *Comparison of the critical strains*

The critical strains from the simulation results were also extracted following the same method as the experimental results. A fall in minimum 0.2 MPa is identified as the occurrence of critical strain. The values of both experimental critical strains and those from the simulations are listed in table 4. Although the actual magnitudes are different but the critical strain values from the simulations are of the same order of magnitude of the critical strains obtained from the experiments. This shows that decent agreement is achieved between the experimental and simulation results for different temperatures and strain rates. Although the curve fitting was done by taking small number of data points and a simpler material model was used, the current material model is found to be more useful over a range of temperatures compared to the work by Maziere *et al* [10] who focused on a single temperature.

6. Conclusion

In this study a DSA material model was fit through the results of tensile tests conducted on SS 316L over a wide range of temperature and strain rates. A new approach was used for fitting the material parameters to the experimental data. Curve fitting was done by taking a much smaller set of the experimental stress-strain data as compared to the earlier work. The model was observed to qualitatively replicate the stress-strain plots at various loading conditions. Critical strains from the simulations were found to be of the same order of magnitude as the experiments.

Acknowledgement

This paper is a revised and expanded version of an article entitled, "Determination of Critical Strain of SS 316L between 450−550°C", Paper No., "150" presented in "First International Conference on Mechanical Engineering" held at 'Jadavpur University', Kolkata, India during January 4-6, 2018.

Nomenclature

Q	Asymptotic value of isotropic hardening stress
Q_{act}	Activation energy
R	Isotropic hardening stress
R_g	Universal gas constant
S	Steady state strain rate sensitivity (SRS)
S_i	Instantaneous SRS
S_a	Aging SRS
S_{OGC}	Oscillating growth criterion
S_{EGC}	Exponential growth criterion
T	Temperature

Greek symbols

ε	Strain
σ	Stress
σ_y	Yield stress
σ_v	Viscoplastic stress
ε_{cr}	Critical strain
Θ	Strain hardening modulus
Δ	Increment

Subscripts

p	Plastic
cr	Critical
a	DSA

References

[1] Van den Beukel A 1975 Theory of the effect of dynamic strain aging on mechanical properties. *Phys. Status Solidi*. 30: 197–206

[2] Zaiser M and Hanher P 1997 Oscillatory modes of plastic deformation: theoretical concepts. *Phys. Status Solidi (B)* 199: 267–330

[3] McCormick P G 1971 The Portevin-Le Chatelier effect in an Al-Mg-Si alloy. *Acta Metall.* 19: 463–471

[4] Bodner S R and Rosen A 1967 Discontinuous yielding of commercially-pure aluminium. *J. Mech. Phys. Solids* 15: 63–67

[5] Penning P 1972 Mathematics of the Portevin-Le Chatelier effect. *Acta Metall.* 20: 1169–1175

[6] Kubin L P and Estrin Y 1985 The Portevin-Le Chatelier effect in deformation with constant stress rate. *Acta Metall*. 33: 397–407

[7] Yaguchi M and Takahashi Y 2000 A viscoplastic constitutive model incorporating dynamic strain aging effect during cyclic deformation conditions. *Int. J. Plast.* 16: 241–262

[8] McCormick P G 1988 Theory of flow localisation due to dynamic strain ageing. *Acre. Metall*. 36: 3061–3067

[9] Zhang S, McCormick P G and Estrin Y 2001 The morphology of Portevin–Le Chatelier bands: finite element simulation for Al–Mg–Si. *Acta. Mater*. 49: 1087–1094

[10] Maziere M and Diereke H 2012 Investigations on the Portevin–Le Chatelier critical strain in an aluminum alloy. *Comput. Mater. Sci.* 52: 68–72

[11] Chaboche J L, Gaubert A, Kanote P, Azzouz F and Maziere M 2013 Viscoplastic constitutive equations of combustion chamber materials including cyclic hardening and dynamic strain aging. *Int. J. Plast*. 46: 1–22

[12] Gopinath K, Gogia A K, Kamat S V and Ramamurty U 2009 Dynamic strain ageing in Ni-base superalloy 720Li. *Acta Mater*. 57: 1243–1253

[13] Ramesh M, Leber H J, Janssens K G F, Diener M and Spolenak R 2011 Thermomechanical and isothermal fatigue behavior of 347 and 316L austenitic stainless tube and pipe steels. Int. *J. Fatigue* 33: 683–691

[14] Jin D, Li J and Shao N 2016 The effect of dynamic strain aging on fatigue property for 316L stainless steel. *J. Mater. Res*. 31: 627–634

[15] Muhamed G A, Gunduz S, Eden M A and Tastemur D 2017 Dynamic strain aging behaviour in AISI 316L austenitic stainless steel under as-received and as-welded conditions. *Metals* 7: 362–376

[16] Hong S G and Lee S B 2004 The tensile and low-cycle fatigue behavior of cold worked 316L stainless steel: influence of dynamic strain aging. *Int. J. Fatigue* 26 :899–910

[17] Shastry C G, Mathew V, Rao K B S and Pathak S D 2007 Tensile deformation behaviour of AISI 316L(N) SS. *Mater. Sci. Technol.* 23: 1215–1222

[18] Gupta A K, Singh S K, Reddy S and Hariharan G 2012 Prediction of flow stress in dynamic strain aging regime of austenitic stainless steel 316 using artificial neural network. *Mater. Des.* 35: 589–595

[19] Jianga H, Chena X, Fana Z, Donga J, Jianga H and Lub S 2009 Influence of dynamic strain aging pre-treatment on creep-fatigue behavior in 316L stainless steel. *Mater. Sci. Eng. (A)* 500: 98–103

[20] Karlsen W, Ivanchenko M, Ehrnsten U, Yagodzinskyy Y and Hanninen H 2009 Microstructural manifestation of dynamic strain aging in AISI 316 stainless steel. *J. Nucl. Mater.* 395: 156–161

[21] Pham M S and Holdsworth S R 2012 Dynamic strain ageing of AISI 316L during cyclic loading at 300°C: Mechanism, evolution, and its effects. *Mater. Sci. Eng. (A)* 556: 122–133

[22] Hong S G and Lee S B 2005 Mechanism of dynamic strain aging and characterization of its effect on the low-cycle fatigue behavior in type 316L stainless steel. *J. Nucl. Mater.* 340: 307–314

[23] Puchi-Cabrera E S 2003 Mechanical behaviour of 316L stainless steel under warm working conditions. *Mater. Sci. Technol.* 19: 189–194

[24] Venkadesan S, Phaniraj C, Sivaprasad P V and Rodriguez P 1992 Activation energy for serrated flow in a 15Cr-15Ni Ti-modified austenitic stainless steel. *Acta Metall. Mater.* 40(3): 569–580

[25] Rodriguez P 1984 Serrated plastic flow. *Bull. Mater. Sci.* 6(4): 653–663

[26] Choudhary B K 2014 Activation energy for serrated flow in type 316L(N) austenitic stainless steel. *Mater. Sci. Eng. (A).* 603: 160–168

[27] Wang W H, Wu D, Chen R S and Lou C S 2015 Influence of temperature and strain rate on serration type transition in NZ31 Mg alloy. *Trans. Nonferr. Met. Soc. China* 25: 3611–3617

[28] Wang W H, Wu D, Shah S S A, Chen R S and Lou C S 2016 The mechanish of critical strain and serration type of the serrated flow in Mg–Nd–Zn alloy. *Mater. Sci. Eng. (A)* 649: 214–221

[29] Bowen A W and Leak G M 1970 Solute diffusion in alpha- and gamma-iron. *Metall. Trans.* 1: 1695–1700

[30] Bohlke T, Bondar G, Estrin Y and Lebyodkin M A 2009 Geometrically non-linear modeling of the Portevin–Le Chatelier effect. *Comput. Mater. Sci*. 44: 1076–1088